

Supporting Information

Efficient electroreduction CO₂ to CO over MnO₂ nanosheets

Xianyun Peng,^{†1} Ying Chen,^{†1} Yuying Mi,[†] Longchao Zhuo,[‡] Gaocan Qi,^{||*} Junqiang Ren,[§] Yuan Qiu,[†]
Xijun Liu^{†*} and Jun Luo[†]

[†] Center for Electron Microscopy and Tianjin Key Lab of Advanced Functional Porous Materials, Institute for New Energy Materials and Low-Carbon Technologies, School of Materials Science and Engineering, Tianjin University of Technology, Tianjin 300384, China.

[‡] School of Materials Science and Engineering, Xi'an University of Technology, Xi'an 710048, China.

^{||} School of Materials Science and Engineering, Tianjin University of Technology, Tianjin 300384, China.

[§] State Key Laboratory of Advanced Processing and Recycling of Nonferrous Metals, Lanzhou University of Technology, Lanzhou 730050, China.

¹ These authors contributed equally to this work.

Corresponding Author: gaocanqi@tjut.edu.cn; xjliu@tjut.edu.cn

Experimental Section

Synthesis of MnO₂ supported on nickel foam

MnO₂ nanosheets supported on Ni foam were synthesized by a simple hydrothermal method. Typically, a piece of nickel foam of (1 cm × 2 cm) was cleaned by a 3 M hydrochloric acid (HCl) aqueous solution, ethanol and deionized water with the assistance of ultrasonication for 15 min to remove the surface impurities and oxide layers. Then, the cleaned nickel foam was placed against the wall of a Teflon lined stainless steel autoclave that contained a homogeneous solution of KMnO₄ (1 mmol) in 30 mL deionized water. Afterward, the autoclave was sealed and maintained at 160 °C for 24 h to synthesize MnO₂ nanosheets arrays. Finally, the Ni foam covered with MnO₂ nanosheets was taken out and cleaned by ultrasonication for three minutes before being fully dried at 80 °C overnight. In this experiment, all the chemical reagents were of analytical purity and used without any further purification.

Material Characterization

Morphologies and microstructures of the as-prepared samples were characterized by using field-emission scanning electron microscopy (FESEM, Quanta FEG 250) and transmission electron microscopy (TEM, FEI Talos F200X). X-ray diffraction measurements (XRD) were performed using an X-ray diffractometer (SmartLab 9 kW) with Cu K α radiation ($\lambda=0.154598$ nm) at a scan rate of 10° min⁻¹ in the 2 θ range from 10° to 90°. Raman spectroscopy measurements were performed with a high-resolution laser confocal microscopy Raman spectrometer (Horiba evolution) with a 532 nm excitation laser. N₂ adsorption-desorption isotherms were measured on a Tristar II 3020 Micromeritics analyzer. Pore volumes and sizes were computed by a quenched solid density functional theory method and specific surface areas were discerned by the Brunauer-Emmett-Teller (BET) method. Atomic force microscope (AFM) images were collected in tapping mode in air by using a Bruker microscope (Dimension icon) and processed using NanoScope Analysis software.

X-ray photoelectron spectroscopy (XPS) measurements were performed with a Kratos AXIS Ultra DLD system with the Al K α radiation as the X-ray source.

Electrochemical CO₂ Reduction Measurements

All electrochemical measurements were carried out at room temperature (25 °C) in a H-type cell with a 0.1 M KHCO₃ solution on an electrochemical workstation (CHI 660D). Platinum foil and a saturated calomel electrode (SCE) were used as the counter and reference electrodes, respectively. The MnO₂-NS/NF with an area of 1 cm \times 1 cm was directly used as the working electrode without any binder or conductive additives. Prior to an experiment, CO₂ was first bubbled into the electrolyte until it was saturated. For the electrochemical tests, a linear sweep voltammetry (LSV) was first carried out to examine the electrochemical activity of the samples at a scan rate of 10 mV s⁻¹ within the voltage range between -1.1 and 0 V. The products and Faradic efficiency of CO₂ reduction were measured using chronoamperometry at each fixed potential. The electrochemically active surface area of the electrode was determined by testing the double layer capacitance, which is derived from the cyclic voltammetry measured at various scan rates. The electrochemical double-layer capacitance (C_{dl}) was estimated by plotting the current density differences against the scan rate. Electrochemical impedance spectroscopy (EIS) was performed in the frequency range from 100 kHz to 10 mHz with an AC amplitude of 5 mV. In this work, all of the measured potentials were referenced to the RHE according to the Nernst equation potential: $E_{RHE}(V) = E_{SCE}(V) + 0.0592 \times pH + 0.241 V$.

Products Analysis

For the identification of the CO₂ reduction products, gas chromatography (GC) and ¹H nuclear magnetic resonance (NMR) analysis were carried out to quantify the gas and liquid products, respectively. The CO product was analyzed at regular time intervals by gas chromatography (Agilent GC-7890) equipped with a Poraplot Q column and a molecular sieve column by a thermal

conductivity detector with N₂ as a carrier gas. The FE of the gas products were calculated by using the concentrations (ppm) detected by the GC as follows equation:

$$FE_{CO} (\%) = (C_{CO} \times V_{CO_2} \times 10^{-3} \times t \times F \times N) / 1344Q$$

where V_{CO_2} is the flow rate of CO₂ (=20 sccm); C_{CO} is the concentration of CO product, based on calibration of the GC; t is electrolysis time (=7200 s); F is the Faraday constant (96485 C mol⁻¹); N is the number of transferred electrons for CO product (=2); Q (C) is the total quantity of electric charge.

¹H NMR spectroscopy was collected on a Bruker AVANCE AV III 400 spectrometer to identify if any liquid-phase CO₂ reduction products. In detail, 0.5 mL electrolyte after electrolysis at the set potential was mixed with 0.1 mL D₂O and 0.03 μL dimethyl sulfoxide (DMSO, 99.99%) as an internal standard. The ¹H spectrum was measured with water suppression using the pre-saturation method.

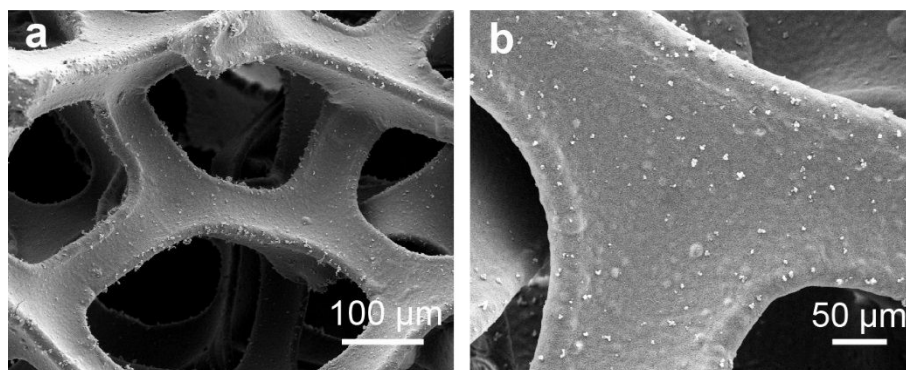


Fig. S1. The low-magnification SEM images of the as-prepared MnO₂ nanosheets.

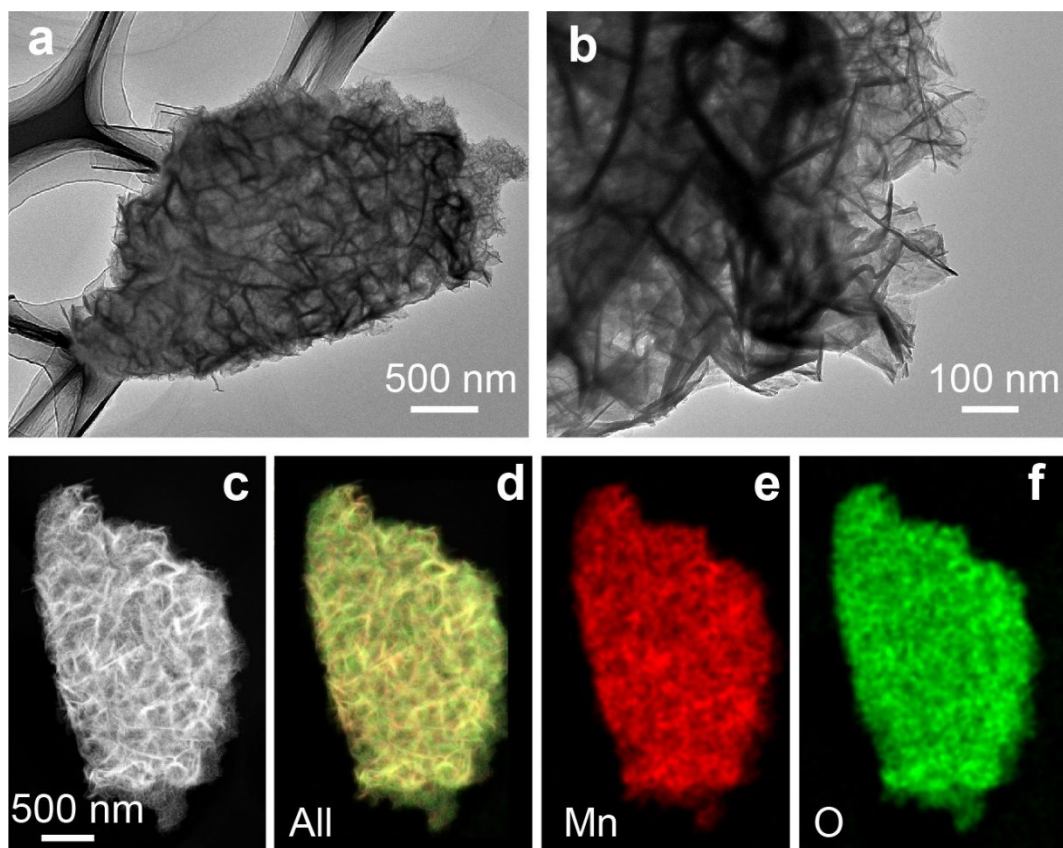


Fig. S2. The microstructure characterization of MnO_2 nanosheets by TEM: (a,b) The low-magnification TEM images; (c-f) High-angle annular dark-field STEM image and the corresponding EDS elemental mapping.

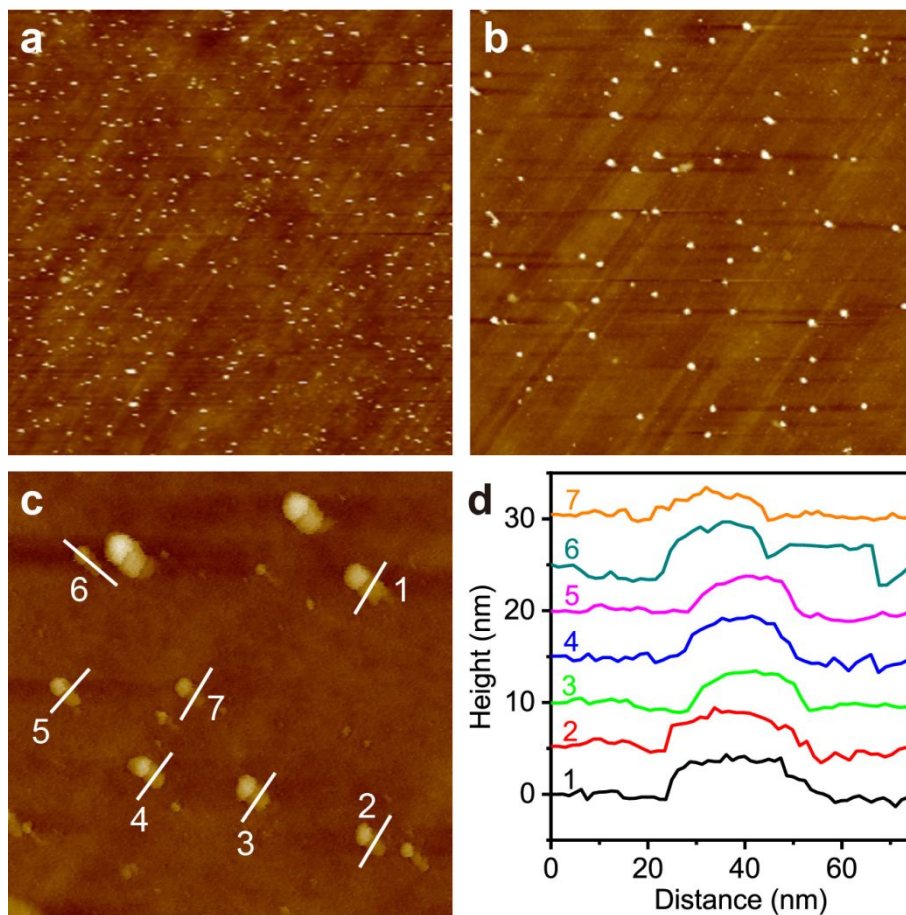


Fig. S3. AFM characterization of the as-prepared MnO₂ nanosheets: (a-c) AFM images of MnO₂ nanosheets; (d) The corresponding height profiles to the AFM images.

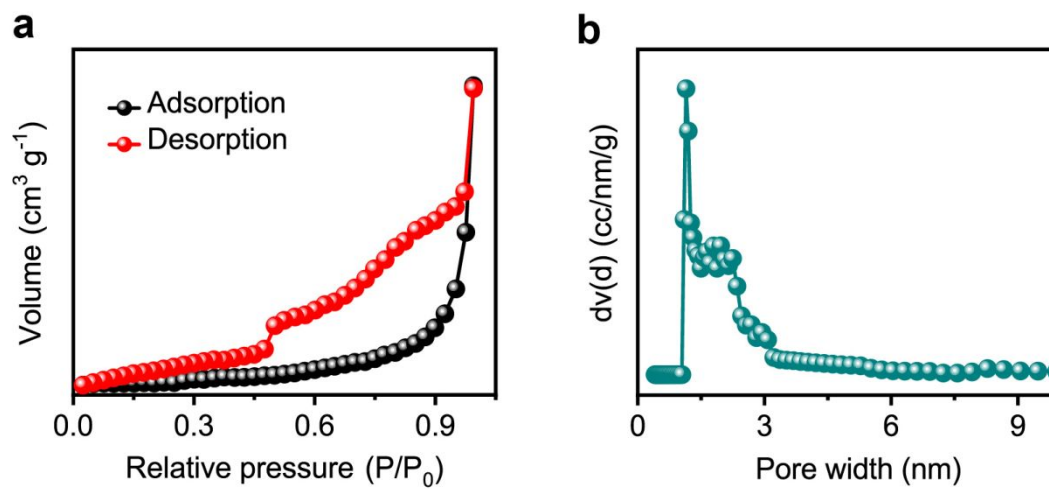


Fig. S4. The BET characterizations of the as-prepared MnO₂-NS/NF: (a) N₂ adsorption-desorption isotherms; (b) Pore size distribution.

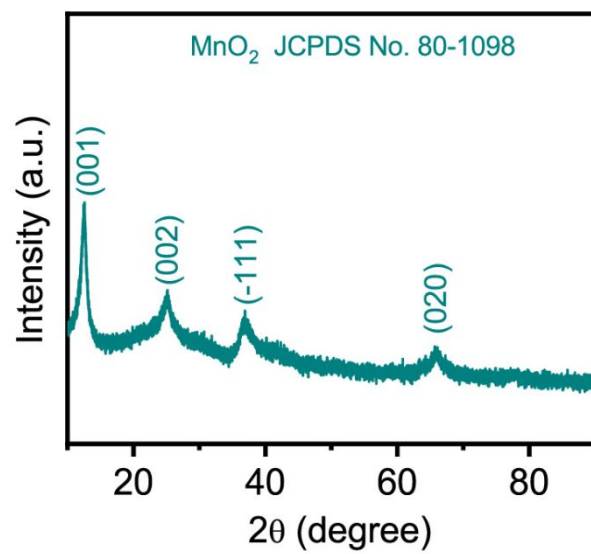


Fig. S5. XRD pattern of commercial MnO_2 .

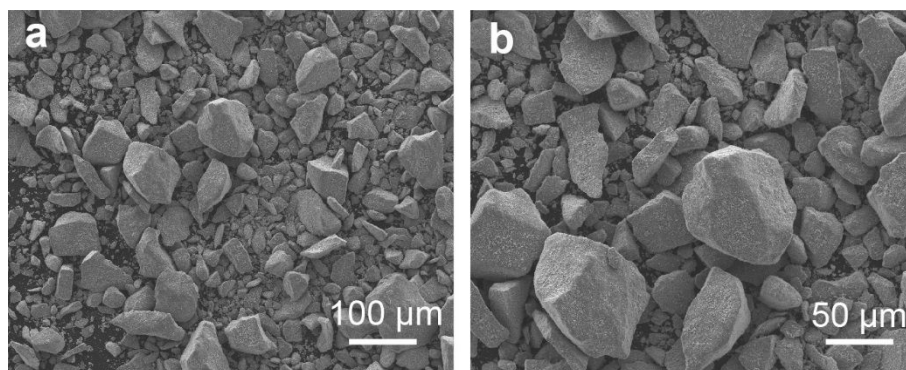


Fig. S6. SEM images of commercial MnO₂.

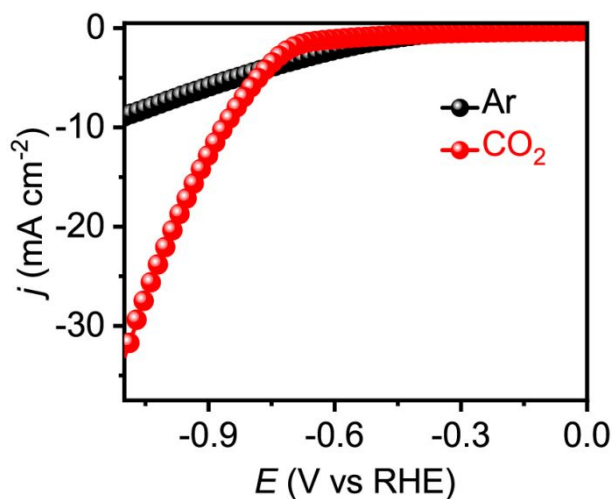


Fig. S7. LSV of the MnO₂-NS/NF catalyst were performed from 0 to -1.1 V in Ar-saturated and CO₂-saturated 0.1 M KHCO₃ electrolyte at a scan rate of 10 mV s⁻¹. Obviously, the MnO₂-NS/NF catalyst shows a much higher current density in CO₂-saturated aqueous solution than that of Ar, demonstrating that the high activity of MnO₂-NS/NF catalyst towards the electrochemical CO₂ reduction. In addition, no any carbonaceous products were detected in Ar-saturated 0.1 M KHCO₃ electrolyte.

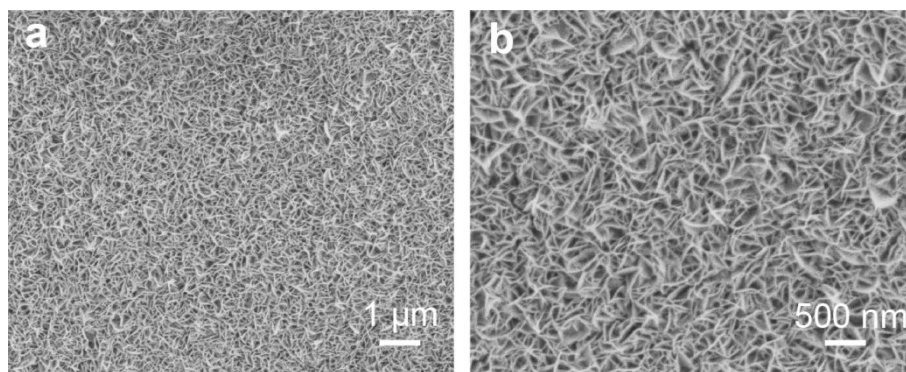


Fig. S8. SEM images of the MnO₂-NS/NF catalyst after the electrolysis.

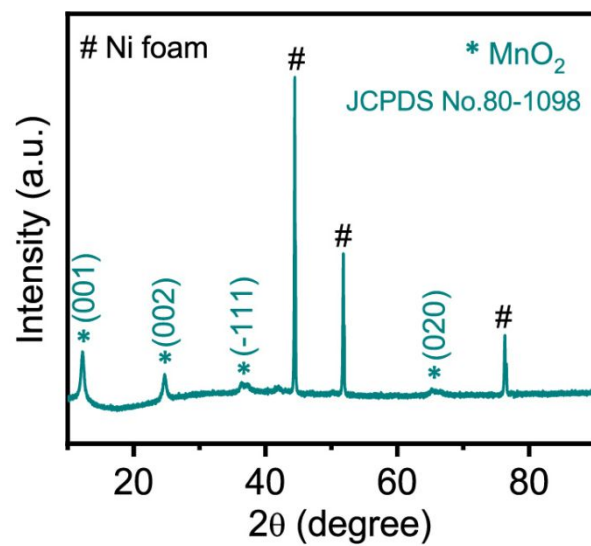


Fig. S9. XRD pattern of the MnO₂-NS/NF catalyst after the electrolysis.

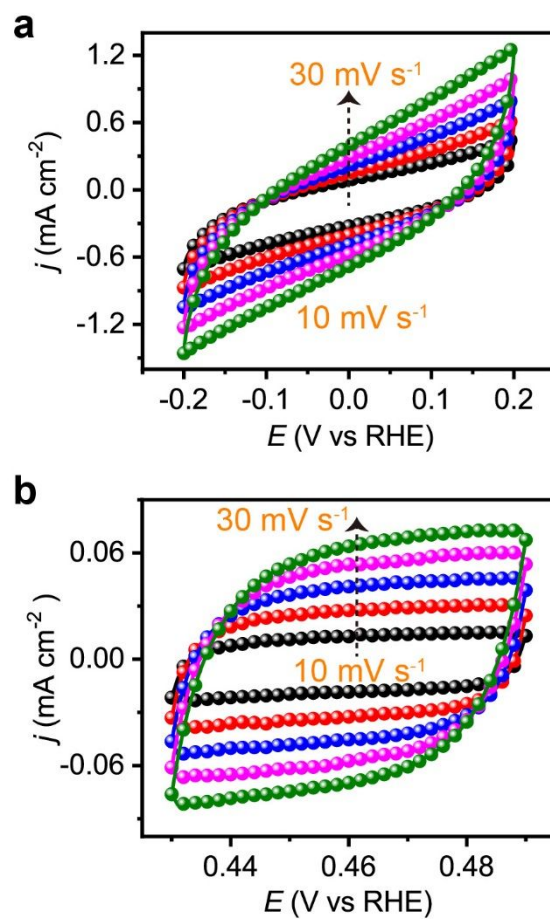


Fig. S10. The electrochemically active surface area characterization: Cyclic voltammetry curves of (a) commercial MnO₂ and (c) MnO₂-NS/NF in non-faradaic capacitance current range at a scan rate of 10, 15, 20, 25, and 30 mV s⁻¹.

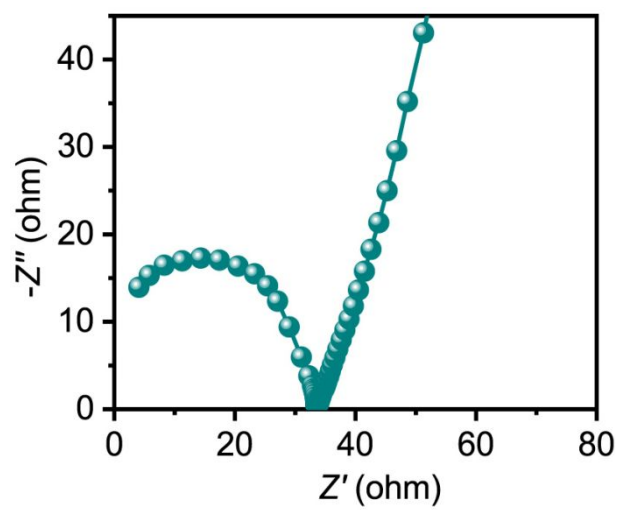


Fig. S11. Nyquist plots of the $\text{MnO}_2\text{-NS/NF}$ catalyst after the electrolysis.

Table S1. CO evolution over noble metal-based electrocatalysts by the electrochemical CO₂ reduction reaction in aqueous electrolytes.

| Catalysts | Electrolyte | FE _{CO} (%) | Current density (mA cm ⁻²) | Potential (V vs. RHE) | Time (h) | Ref. |
|--------------------------|-------------------------|-------------------------|---|--------------------------|-------------|------|
| 5 nm Ag/C | 0.5 M KHCO ₃ | 79.2 | 0.23 | -0.75 | - | 1 |
| Au-CeO _x /C | 0.1 M KHCO ₃ | 89.1 | 12.9 | -0.89 | 10.3 | 2 |
| Oxide-derived Ag | 0.1 M KHCO ₃ | 89 | 1.15 | -0.8 | - | 3 |
| Oxide-derived Au | 0.5 M KHCO ₃ | 96 | ~3.8 | -0.35 | 8 | 4 |
| Au nanoparticles | 0.5 M KHCO ₃ | 97 | - | -0.52 | 0.5 | 5 |
| Oxygen plasma-treated Ag | 0.1 M KHCO ₃ | 90 | - | -0.6 | 3 | 6 |
| Ultrathin Au Nanowires | 0.5 M KHCO ₃ | 94 | 8.16 | -0.35 | 6 | 7 |
| Au/Cu Nanoparticles | 0.1 M KHCO ₃ | ~94 | ~3.5 | -0.8 | 12 | 8 |

| | | | | | | |
|----------------------------------|-------------------------|------|------|-------|-----|----|
| Nanoporous Ag | 0.5 M KHCO ₃ | 93.1 | 37.3 | -0.8 | 2 | 9 |
| Triangular Ag Nanoplates | 0.1 M KHCO ₃ | 96.8 | ~2 | -0.86 | 168 | 10 |
| SnO_x/Ag | 0.5 M KHCO ₃ | 85 | ~1 | -0.6 | - | 11 |
| 3.7 nm Pd nanoparticles | 0.1 M KHCO ₃ | 91.2 | ~9 | -0.89 | - | 12 |
| Pd icosahedra/C | 0.1 M KHCO ₃ | 91.1 | ~2 | -0.8 | 10 | 13 |
| 4.5 nm Pd/PdO_x | 0.5 M KHCO ₃ | 90 | 2.53 | -0.55 | 24 | 14 |
| Pd nanosheets | 0.1 M KHCO ₃ | 94 | 400 | -0.9 | 8 | 15 |
| Ag-IO | 0.1 M KHCO ₃ | 80 | - | - | - | 16 |
| Cu-Ag | 0.5 M KHCO ₃ | 95.7 | 27.3 | -1.0 | 14 | 17 |
| PD-Ag | 0.5 M KHCO ₃ | 97.3 | 2.93 | -0.7 | 10 | 18 |

References

- [1] Kim, C.; Jeon, H. S.; Eom, T.; Jee, M. S.; Kim, H.; Friend, C. M.; Min, B. K.; Hwang, Y. J. Achieving selective and efficient electrocatalytic activity for CO₂ reduction using immobilized silver nanoparticles. *J. Am. Chem. Soc.* **2015**, *137*, 13844–13850.
- [2] Gao, D.; Zhang, Y.; Zhou, Z.; Cai, F.; Zhao, X.; Huang, W.; Li, Y.; Zhu, J.; Liu, P.; Yang, F.; Wang, G.; Bao, X. Enhancing CO₂ electroreduction with the metal-oxide interface. *J. Am. Chem. Soc.* **2017**, *139*, 5652–5655.
- [3] Ma, M.; Trzesniewski, B. J.; Xie, J.; Smith, W. A. Selective and efficient reduction of carbon dioxide to carbon monoxide on oxide-derived nanostructured silver electrocatalysts. *Angew. Chem. Int. Ed.* **2016**, *55*, 9748–9752.
- [4] Chen, Y.; Li, C. W.; Kanan, M. W. Aqueous CO₂ reduction at very low overpotential on oxide-derived Au nanoparticles. *J. Am. Chem. Soc.* **2012**, *134*, 19969–19972.
- [5] Zhu, W.; Michalsky, R.; Metin, O.; Lv, H.; Guo, S.; Wright, C. J.; Sun, X.; Peterson, A. A.; Sun, S. Monodisperse Au nanoparticles for selective electrocatalytic reduction of CO₂ to CO. *J. Am. Chem. Soc.* **2013**, *135*, 16833–16836.
- [6] Mistry, H.; Choi, Y. W.; Bagger, A.; Scholten, F.; Bonifacio, C. S.; Sinev, I.; Divins, N. J.; Zegkinoglou, I.; Jeon, H. S.; Kisslinger, K.; Stach, E. A.; Yang, J. C.; Rossmeisl, J.; Roldan Cuenya, B. Enhanced carbon dioxide electroreduction to carbon monoxide over defect-rich plasma-activated silver catalysts. *Angew. Chem. Int. Ed.* **2017**, *56*, 11394–11398.
- [7] Zhu, W.; Zhang, Y. J.; Zhang, H.; Lv, H.; Li, Q.; Michalsky, R.; Peterson, A. A.; Sun, S. Active and selective conversion of CO₂ to CO on ultrathin Au nanowires. *J. Am. Chem. Soc.* **2014**, *136*, 16132–16135.
- [8] Kauffman, D. R.; Alfonso, D. R.; Tafen, D. N.; Wang, C.; Zhou, Y.; Yu, Y.; Lekse, J. W.; Deng, X.; Espinoza, V.; Trindell, J.; Ranasingha, O. K.; Roy, A.; Lee, J.-S.; Xin, H. L. Selective electrocatalytic reduction of CO₂ into CO at small, thiol-capped Au/Cu nanoparticles. *J. Phys. Chem. C* **2018**, *122*, 27991–28000.
- [9] Lu, Q.; Rosen, J.; Zhou, Y.; Hutchings, G. S.; Kimmel, Y. C.; Chen, J. G.; Jiao, F. A selective and efficient electrocatalyst for carbon dioxide reduction. *Nat. Commun.* **2014**, *5*, 3242.
- [10] Liu, S.; Tao, H.; Zeng, L.; Liu, Q.; Xu, Z.; Liu, Q.; Luo, J. L. Shape-dependent electrocatalytic reduction of CO₂ to CO on triangular silver nanoplates. *J. Am. Chem. Soc.* **2017**, *139*, 2160–2163.
- [11] Cai, Z.; Wu, Y.; Wu, Z.; Yin, L.; Weng, Z.; Zhong, Y.; Xu, W.; Sun, X.; Wang, H. Unlocking bifunctional electrocatalytic activity for CO₂ reduction reaction by win-win metal–oxide cooperation. *ACS Energy Lett.* **2018**, *3*, 2816–2822.

- [12] Gao, D.; Zhou, H.; Wang, J.; Miao, S.; Yang, F.; Wang, G.; Wang, J.; Bao, X. Size-dependent electrocatalytic reduction of CO₂ over Pd nanoparticles. *J. Am. Chem. Soc.* **2015**, *137*, 4288-4291.
- [13] Huang, H.; Jia, H.; Liu, Z.; Gao, P.; Zhao, J.; Luo, Z.; Yang, J.; Zeng, J. Understanding of strain effects in the electrochemical reduction of CO₂: using Pd nanostructures as an ideal platform. *Angew. Chem. Int. Ed.* **2017**, *56*, 3594–3598.
- [14] Lu, H.; Zhang, L.; Zhong, J. H.; Yang, H. G. Partially oxidized palladium nanodots for enhanced electrocatalytic carbon dioxide reduction. *Chem-Asian J.* **2018**, *13*, 2800–2804.
- [15] Zhu, W.; Zhang, L.; Yang, P.; Hu, C.; Luo, Z.; Chang, X.; Zhao, Z. J.; Gong, J. Low-coordinated edge sites on ultrathin palladium nanosheets boost carbon dioxide electroreduction performance. *Angew. Chem. Int. Ed.* **2018**, *57*, 11544–11548.
- [16] Yoon, Y.; Hall, A. S.; Surendranath, Y. Tuning of silver catalyst mesostructure promotes selective carbon dioxide conversion into fuels. *Angew. Chem.* **2016**, *128*, 15508–15512.
- [17] Urbain, F.; Tang, P.; Carretero, N. M.; Andreu, T.; Arbiol, J.; Morante, J. R. Tailoring copper foam with silver dendrite catalysts for highly selective carbon dioxide conversion into carbon monoxide. *ACS Appl. Mater. Interfaces* **2018**, *10*, 43650–43660.
- [18] Gao, J.; Zhu, C.; Zhu, M.; Fu, Y.; Huang, H.; Liu, Y.; Kang, Z. Highly selective and efficient electroreduction of carbon dioxide to carbon monoxide with phosphate silver-derived coral-like silver. *ACS Sustain. Chem. Eng.* **2019**, *7*, 3536–3543.